



## **A high-performance lab-on-a-chip liquid sensor employing surface acoustic wave resonance: part II**

Downloaded from: <https://research.chalmers.se>, 2024-04-25 12:28 UTC

Citation for the original published paper (version of record):

Kustanovich, K., Yanchev, V., Olivefors, A. et al (2019). A high-performance lab-on-a-chip liquid sensor employing surface acoustic wave resonance: part II. Journal of Micromechanics and Microengineering, 29(2).  
<http://dx.doi.org/10.1088/1361-6439/aaf411>

N.B. When citing this work, cite the original published paper.

PAPER • OPEN ACCESS

## A high-performance lab-on-a-chip liquid sensor employing surface acoustic wave resonance: part II

To cite this article: K Kustanovich *et al* 2019 *J. Micromech. Microeng.* **29** 024001

View the [article online](#) for updates and enhancements.



**IOP | ebooks™**

Bringing you innovative digital publishing with leading voices to create your essential collection of books in STEM research.

Start exploring the **collection** - download the first chapter of every title for free.

# A high-performance lab-on-a-chip liquid sensor employing surface acoustic wave resonance: part II

K Kustanovich<sup>✉</sup>, V Yantchev<sup>✉</sup>, A Olivefors, B Ali Doosti<sup>✉</sup>, T Lobovkina and A Jesorka

Biophysical Technology Laboratory, Department of Chemistry & Chemical Engineering, Chalmers University of Technology, Kemivägen 10, Göteborg 412 96, Sweden

E-mail: [ventsi.yantchev@gmail.com](mailto:ventsi.yantchev@gmail.com)

Received 31 July 2018, revised 18 November 2018

Accepted for publication 26 November 2018

Published 3 January 2019



## Abstract

We recently introduced an in-liquid sensing concept based on surface acoustic resonance (SAR) in a lab-on-a-chip resonant device with one electrical port. The 185 MHz one-port SAR sensor has a sensitivity comparable to other surface acoustic wave (SAW) in-liquid sensors, while offering a high quality factor (Q) in water, low impedance, and fairly low susceptibility to viscous damping. In this work, we present significant design and performance enhancements of the original sensor presented in part I. A novel ‘lateral energy confinement’ (LEC) design is introduced, where the spatially varying reflectivity of the SAW reflectors enables strong SAW localization inside the sensing domain at resonance. An improvement in mass-sensitivity greater than 100% at resonance is achieved, while the measurement noise stays below 0.5 ppm. Sensing performance was evaluated through real-time measurements of the binding of 40 nm neutravidin-coated SiO<sub>2</sub> nanoparticles to a biotin-labeled lipid bilayer. Two complementary sensing parameters are studied, the shift of resonance frequency and the shift of conductance magnitude at resonance.

Keywords: microfluidics, surface acoustic wave, sensor, resonance, biochemical

(Some figures may appear in colour only in the online journal)

## 1. Introduction

Over the last three decades, electroacoustic (EA) and microfluidic technologies have emerged as versatile complementary components of miniaturized analytical devices. The rapid advance of the lab-on-a-chip concept (i.e. integrated sample preparation and analytical back-end) has further elevated the interest in combining these two technological fields. Lab-on-a-chip systems have several advantages over conventional laboratory techniques used in analytical chemistry and life sciences: the devices are small, low cost and often disposable, capable of multi-step automation, resulting in fast turnaround

and automation. Additionally, they make it possible to reduce the amount of reagent and sample consumption, while maintaining precise control over the environment.

In this context, small, cheap and efficient sensors capable of in-liquid operation are in great demand. The introduction of acoustic wave technology onto lab-on-a-chip platforms provides sensing capability that meets these criteria and offers an extended set of sample preparation functions to be implemented, such as fast fluidic actuation, contact-free particle manipulation, and sorting.

The majority of acoustic-wave biochemical sensors have to be immersed in aqueous solutions in order to deliver the analyte to the sensing surface in a compatible fluid environment. Acoustic sensors that are commonly used in gas-chemical and biochemical applications typically rely on gravimetric analysis—one of the most explored sensing concepts in chemical



Original content from this work may be used under the terms of the [Creative Commons Attribution 3.0 licence](https://creativecommons.org/licenses/by/3.0/). Any further distribution of this work must maintain attribution to the author(s) and the title of the work, journal citation and DOI.

analysis. In this context, an essential requirement on the sensor is that it preserves its functionality when immersed in fluid and reliably detects mass changes due to a specific (bio)chemical reaction on the sensing surface. To supply and confine the analyte to the sensing area and at the same time protect these devices from the liquid environment, a soft polymer microfluidic delivery system is often used [1].

Significant efforts in the field of microfluidics-integrated sensing technology have focused on the development of highly sensitive, label-free, real-time devices based on the thin-film EA technology. Microsystems based on this approach have a particularly strong potential for commercialization, enabled by the fabrication technologies established by the radio frequency (RF) filter industry. Thickness-excited quasi-shear film bulk acoustic resonators (shear-FBARs) have shown the best performance so far [2, 3]. This is currently the only device type that has reached the stage of commercial prototypes. Thin-film S<sub>0</sub>-Lamb waves and their equivalent extensional plate modes have also shown to be promising, since they also rely on the technology originally developed for commercial RF filter manufacturing [4]. However, these approaches are limited by practical considerations concerning process uniformity, device fragility, strong local pressure and temperature sensitivity [3].

So far, the majority of surface acoustic wave (SAW) devices has been used in the telecommunication industries for RF filtering and signal processing applications, but SAW technology is gaining more and more attention in the microfluidics community. Recent research has already demonstrated that SAW technology provides an effective means of controlling, sensing and actuating particles and fluids in lab-on-a-chip systems [1]. Thus, this platform concept is generating increasing attention, and much effort has been put forward to bring the technology to commercial viability, mainly aiming at applications in medical diagnostics.

SAW-based sensors mostly rely on delay-line configurations where the SAW propagates through a comparatively long distance between input and output transducers to accumulate sufficient time delay and phase shift [5, 6]. However, for in-liquid operation, SAW delay line biosensors are characterized by strong signal loss in transmission, and relatively large size. To address these issues, a two-port SAW resonator with smaller distance between the transducers was introduced as an alternative to the delay line concept [7]. Despite all the benefits provided by this approach, the two-port configuration is somewhat problematic when parallelization needs to be considered. For that reason, one-port sensor systems have been developed.

We have earlier proposed the concept of surface acoustic resonance (SAR) by constructing a proof of principle microfluidic sensor in one-port configuration (Part I) [8]. In this work, the reflective gratings of a one-port SAW resonator are employed as mass loading-sensing elements, with the SAW transducer being protected from the measurement environment and acting only as a read-out element. The concept of separate driving and sensing units was for the first time implemented in SAW sensor technology.

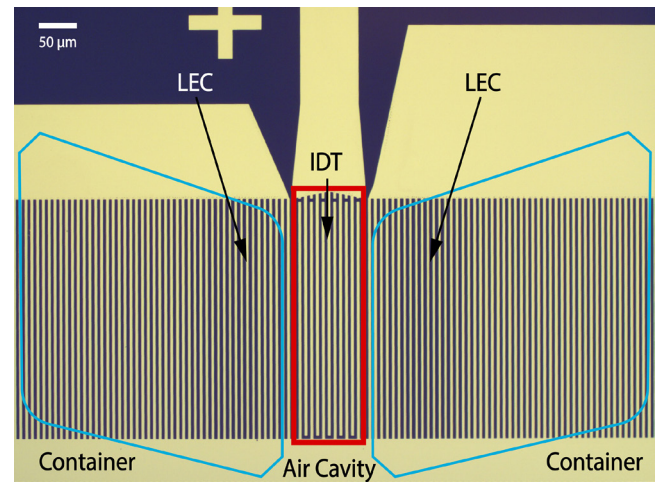


**Figure 1.** SAR sensor employing lateral energy confinement, placed at the bottom of the liquid containers (blue outlines). The outline of the air cavity above the IDT is depicted in red. The LEC regions are highlighted.

Here, we redesigned the topology of the sensor and introduced a ‘lateral energy confinement’ (LEC) to our sensor, enhancing the device sensitivity to approach closer the theoretical limit of the shear SAW. The newly designed sensors are characterized in time-resolved measurements and compared to the proof-of-principle design presented in part I. The microfabrication process remained unchanged; it has been previously presented [8] and is not further elaborated here.

## 2. The ‘LEC’ concept

The enhanced SAR sensor employs the reflective gratings of the one-port SAW resonator as sensing elements, while the transducer is a wide-band interdigital transducer (IDT), placed in-between the reflectors and protected from the liquid by an air cavity. The sensitivity of the SAW resonance is determined primarily by the changes in SAW propagation when propagating under the reflective gratings subjected to viscoelastic load. In our original SAR sensor design (Part I) the SAW energy is being gradually reflected back to the IDT, thus promoting strong SAW localization under the IDT, while outside the transducer the SAW displacement is exponentially decaying. This effect itself is limiting the device sensitivity, since it is determined by the ratio between the kinetic energy at the sensing surface and the total kinetic energy in the system [9]. Typically, an improvement in SAW sensitivity results from better confinement of SAW energy near the surface, achieved through slowing down the wave [8, 10].

We now address the sensitivity limitation imposed by the decaying nature of the SAW inside the sensing area, i.e. reflectors, by introducing a lateral SAW localization through a specially designed SAW energy confinement topology. The concept of the ‘LEC’ design is shown as fabricated in figure 1. It utilizes the same material stack and grating pitch as in our earlier conceptual design presented in Part I [8]. Here, a variation of grating reflectivity is introduced to confine a larger amount of SAW energy in the sensing containers. We establish

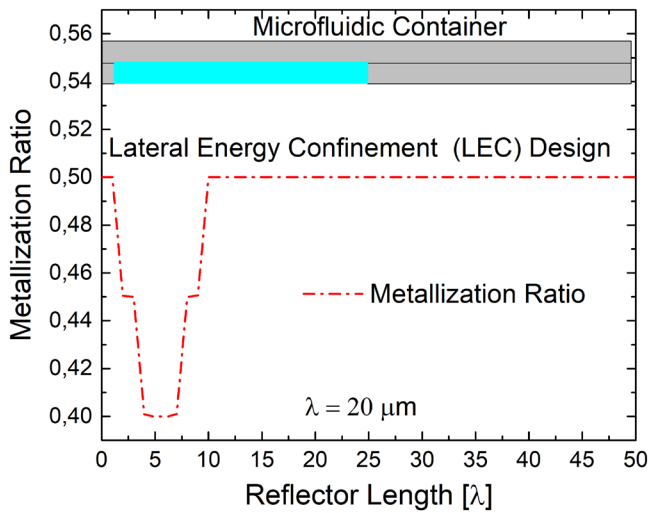


**Figure 2.** Lateral modulation of the mark-to-pitch ratio of the grating strip defining the acoustic wave confinement regions. The top section of the image shows schematically the position of the polymer part of the device, with the light blue part being the liquid-filled container.

a domain of reduced reflectivity just beside the IDT that enables significant amount of SAW energy to be concentrated in the sensing domain at resonance. The reduction of grating reflectivity is achieved through an area characterized by narrower grating strips, i.e. strips with a smaller mark-to-pitch ratio. In figure 2 the specific variation of the mark-to-pitch ratio is shown. In the earlier SAR sensor design, the mark-to-pitch ratio was  $m = 0.5$  for all strips in the reflector grating, while here it narrows locally to  $m = 0.4$  forming two energy localization domains centered at about 5 wavelengths from the IDT ends. The IDT consists of 7 pairs of electrodes for wideband operation, while the device aperture is  $20\lambda$ , with  $\lambda = 20 \mu\text{m}$  at resonance.

A 2D COMSOL Multiphysics® (Version 5.3) frequency response analysis of the proposed SAR device was performed to verify and reveal the fundamentals of the LEC performance. In figure 3, the transversal shear displacement distributions are shown as simulated at resonance for three different designs of the LEC topology. All designs follow the scheme in figure 2 with the difference in the minimum metallization ratio inside the LEC zone, while the smooth acoustic impedance transition to it is provided by two pairs of grating strips with their metallization ratios derived as the mean value of the minimum and maximum metallization ratios.

The applied design scheme promotes energy confinement at the sensing surface within the containers. Lower minimum metallization ratios in the LEC domain ensure greater SAW confinement in the sensing area at the expense of coupling between the IDT and the SAW. The SAR sensor concept relies on both the ability of the IDT to probe sensitivity of the reflector gratings and the ability of the IDT to introduce sufficient energy into the sensing domain. In fact, there has to be a fine balance between these two requirements. For example, a SAR sensor with a very long IDT will have most of its energy under the IDT, and will not be able to sense outside of it. On the other hand, if energy confinement in the reflectors is too

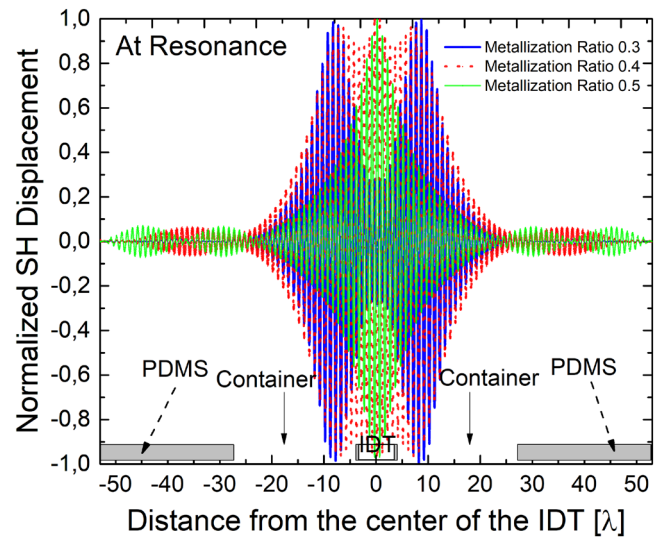


**Figure 3.** Normalized SH-SAW displacement distributions at resonance. The bottom part shows the positions of the microfluidic chip cavities above IDT and reflectors. At  $m = 0.5$ , there is no energy localization. At  $m = 0.4$ , energy localization in containers can be observed, while IDT remains strongly coupled with the system. At  $m = 0.3$ , most of energy is localized in containers, while IDT decouples from the system as can be observed from a low amplitude region next to it.

strong, most of the SAW energy will remain there, and as a result decouple from the IDT. Accordingly, in both extreme cases either the sensitivity or the electrical response of the device become poor.

To further study the optimal LEC design we simulated sensitivity and magnitude of the device response as a function of energy localization in the LEC domain. The sensor response was studied by applying a mass load over the container region of the resonator. We have used shell elements in COMSOL to introduce this mass load as a boundary condition. In figure 4, normalized sensitivity and normalized magnitude of conductance are shown in a comparative manner for the LEC domains with a varying minimum metallization ratio. As expected, the device sensitivity exhibits a maximum determined by the trade-off between the energy confinement in the sensing domain and the IDT coupling to the SAW at resonance. Below a metallization ratio of 0.4, the IDT coupling rapidly decreases, which in turn determines its poorer probing abilities and thus reduced device sensitivity.

By contrast, at antiresonance the energy is confined predominantly under the IDT in all LEC designs, while the SAW amplitude is decaying along the reflector grating (figure 5).

Both modes of operation were compared experimentally with respect to their sensitivity. In figure 6 the conductance around resonance, and the resistance around antiresonance are shown as measured in air and water. The resonance frequency is approximately 188 MHz. A frequency shift of the conductance peak of about  $-2200 \text{ ppm}$  is observed as a result of water loading, accompanied by a 27% decrease of the conductance peak magnitude. Note that the sensitivities demonstrated at resonance in the original design (Part I) were  $-915 \text{ ppm}$  and  $-5\%$ , respectively, while the maximum sensitivity was theoretically estimated to be about  $-2100 \text{ ppm}$  [8].



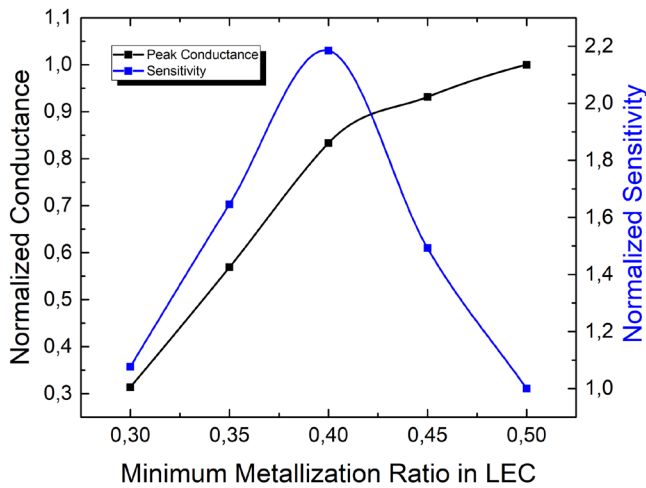


**Figure 4.** Normalized conductance and sensitivity at different metallization ratios.

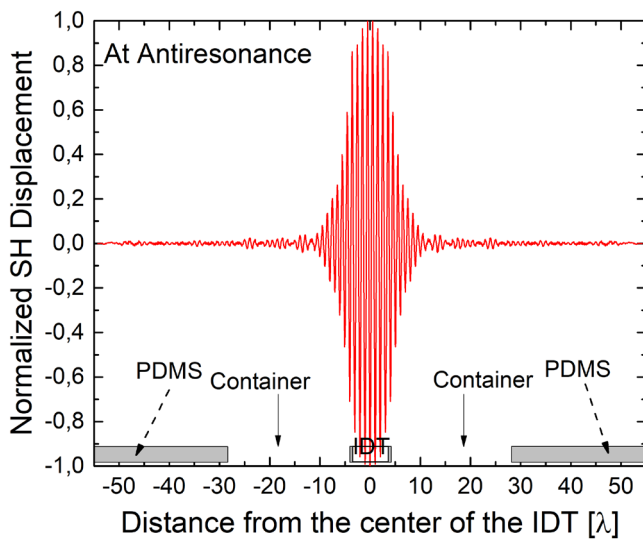


**Figure 5.** Normalized SH-SAW displacement distribution at antiresonance for  $m = 0.4$ . The bottom part shows the positions of the microfluidic chip cavities above IDT and reflectors.

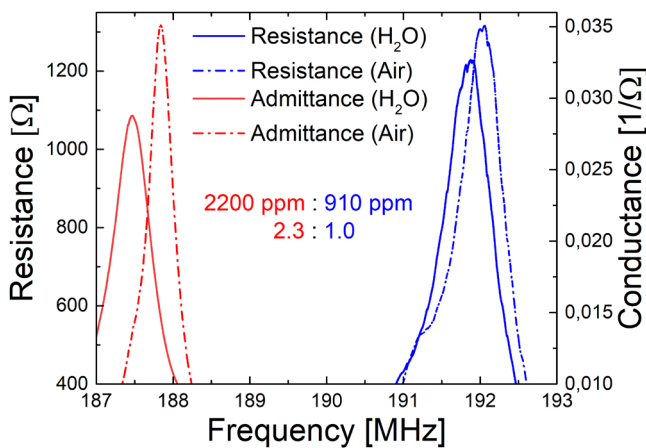


**Figure 6.** SAR sensor performance under water load. Admittance and Resistance are depicted in red and blue, respectively. Dash-dotted lines represent water samples, and solid lines air samples for comparison.

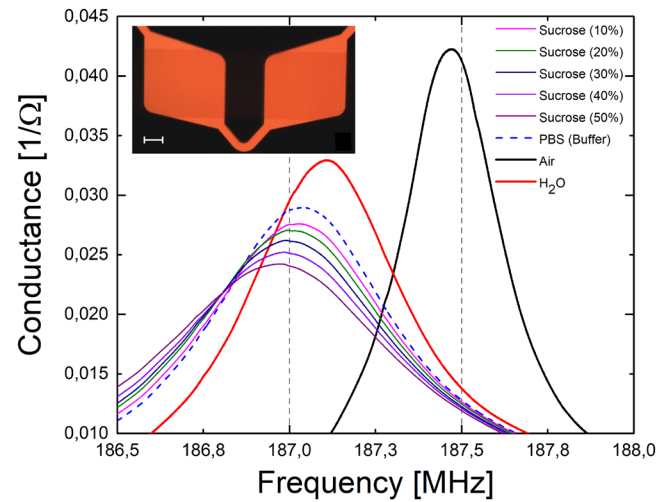


**Figure 7.** SAR sensor performance under viscous load. The colored graphs represent the signals of different sucrose solution loads, the dashed line belongs to the buffer reference (0% sucrose), and the black line is the signal of the empty containers. The inset shows a fluorescence micrograph of the microfluidic chambers and flow channels, loaded with fluorescent nanoparticles. The scale bar represents 100  $\mu\text{m}$ .

**Table 1.** Table of sensor sensitivity under various loads.

Sensor load	Original (part I)	Improved
Air to water	−915 ppm	−2200 ppm
Water to PBS	−160 ppm	−315 ppm
PBS to 20% Sucr.	−160 ppm	−220 ppm
PBS to 40% Sucr.	−260 ppm	−600 ppm
PBS to 50% Sucr.	−450 ppm	−960 ppm

The difference in the measured sensitivities between the original design (Part I) and the LEC design is in excellent agreement with theoretical predictions. Accordingly, the optimized LEC design enables a significant improvement in device sensitivity.

At antiresonance the observed frequency shift of the resistance peak of about −910 ppm determines a sensitivity which is 2.3 times smaller than the sensitivity of the resonance. This again demonstrates the impact of the energy distribution on the device sensitivity.

### 3. Results and discussion

#### 3.1. In-liquid sensor characterization

The SAR sensor has been characterized in an environment with a varying (viscosity  $\times$  density) product ( $\rho\eta$ ) using the Planar 304/1 (Copper Mountain Technologies, USA) vector network analyzer with a set of measurement probes (Picoprobe, Model 40A, GGB Industries Inc., USA). Sucrose solutions of up to 50% content in phosphate buffer saline (PBS) have been evaluated (figure 7). The SAR sensor tolerates the viscous damping well, exhibiting about 17% decrease in conductance peak magnitude for Sucrose-PBS solutions of up to 50%. The observed attenuation is about three times higher than that of the original design (Part I) [8], which is related to the increase

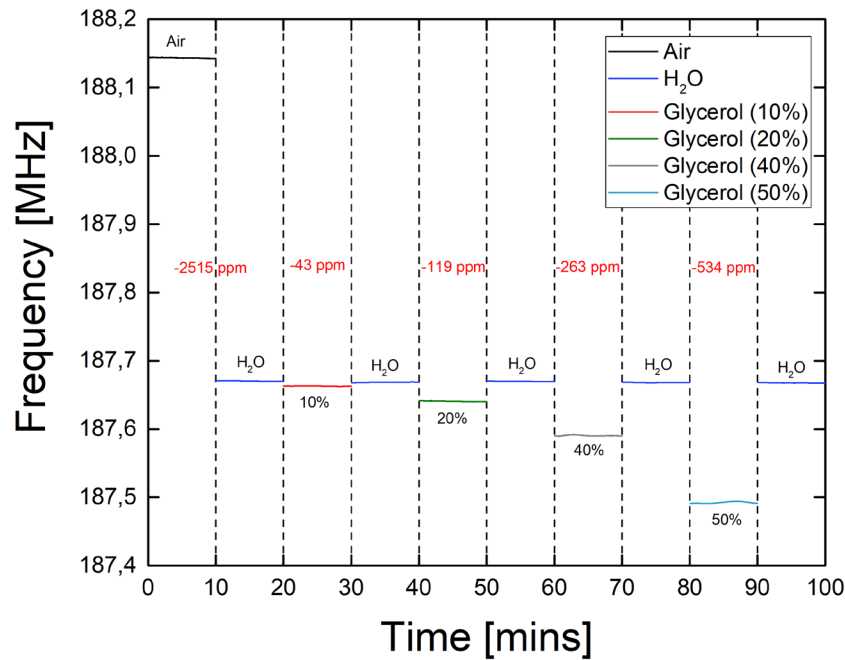


**Figure 8.** Time-resolved response of the SAR sensor under viscous load. The colors encode the signals for air (grey), water (blue) and sucrose loads of different concentrations. Frequency shifts per time step are indicated in red.

in sensitivity demonstrated by the new design. Note that the attenuation is still within acceptable limits, low impedance at resonance is retained. In table 1 the demonstrated frequency sensitivity is presented as compared to the original SAR design (Part I) [8]. An overall two-fold increase in sensitivity is apparent.

These results can be readily compared to the state-of-art in-liquid sensors. The response of the 187 MHz SAR sensor at 40% sucrose corresponds to a square root of the viscosity  $\times$  density product  $(\rho\eta)^{0.5}$  of about 2.3 times the value of PBS ( $\sim 1 \text{ kg} \times \text{m}^{-2} \text{ s}^{-0.5}$ ). For such a variation, a 900 MHz FBAR has demonstrated the same sensitivity of about  $-600 \text{ ppm}$  [11]. The improved SAR sensor design demonstrates a sensitivity comparable to FBAR at an almost 5 times lower frequency. It is noted that the shear wave sensitivity scales with the square root of the operating frequency. On the other hand, the noise levels also increase with frequency, which has an impact on sensor resolution. In addition, high frequency devices are much more susceptible to parasitic effects and instabilities [12].

A SAW delay line, operating at 100 MHz, has demonstrated a frequency shift of about  $-500 \text{ ppm}$ , corresponding to a change of  $(\rho\eta)^{0.5}$  from 1 to 4.35 [13]. The measured 187 MHz SAR sensor response for the same change is about  $-960 \text{ ppm}$  (50% Sucrose solution), which is significantly larger than the effect of frequency scaling ( $f^{0.5} \sim 1.37$  times).

Time-resolved measurements were performed to investigate the sensor recovery and the measurement noise. In figure 8, measurement results of different concentrations of glycerol in water are presented. In this set of measurements, water is used to establish the base sensor response level after each individual measurement of glycerol solution. The results show that, when water is introduced to the sensor containers, the resonant frequency recovers repeatedly to the initial value,

providing a stable baseline. When the sensor is exposed to glycerol solutions, the resonant frequency decreases to a concentration-dependent value, which remains unchanged over the measurement window, indicating sufficient stability of the SAR sensor for practical purposes.

The noise level was calculated using averaging of the Allan deviation  $\sigma$  over 10 min. Each  $\sigma$  was derived from 200 subsequent measurements at 3 s intervals with the VNA at 3 dBm input power. The measured conductances were fitted near resonance to a 5th order polynomial, and the resonance frequencies were subsequently extracted from the polynomial fit of each measurement. Noise levels under load were determined over 10 min to be below 0.5 ppm for resonance frequencies, and below 10 ppm for the conductance peak. This number determines the limit of frequency detection ( $3\sigma < 1.5 \text{ ppm}$ ) and the limit of conductance magnitude detection ( $3\sigma < 30 \text{ ppm}$ ). Further improvement in the limit of frequency detection is possible through an increase of the input power of the VNA used in the measurements, and through ensuring better thermal stability of the physical measurement environment. We also note that despite being from the same batch/wafer, each individual chip has tolerances within a few percent of the nominal value due to a technological drift. These drifts usually exist between different devices and are readily compensated by calibration routines.

### 3.2. Biochemical sensing

For further characterization of the SAR sensor we performed sensing of lipid film-nanoparticle-interactions, using a protocol similar to the one established in part I (figure 9) [8]. We deposited, in a two-step experiment using a microfluidic chamber at 21 °C, a biotin-modified supported lipid bilayer (SLB) over the reflector areas, followed by neutravidin-coated

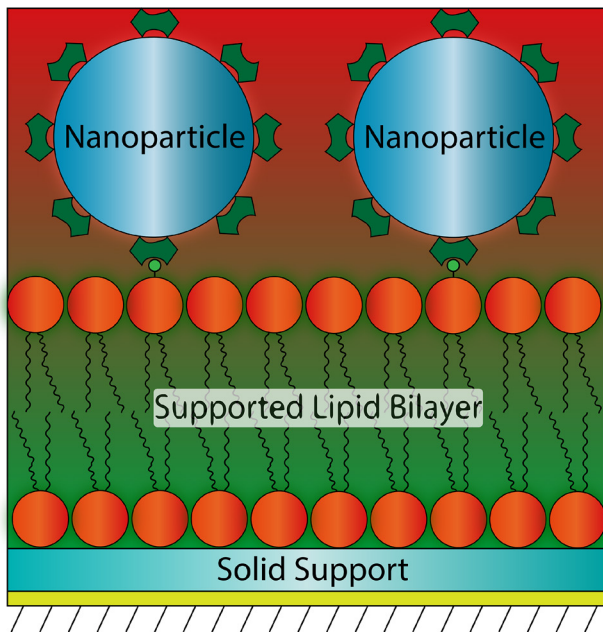


**Figure 9.** Schematic representation (not to scale) of the molecular interactions employed in the neutravidin-biotin-based nanoparticle-lipid bilayer assay. The protein-coated nanoparticles establish an affinity-based association with biotinylated lipids present at 5% (w/w) in the bilayer. Note that the neutravidin has four binding sites for biotin. The solid support is the silicon dioxide top coating of the SAR sensor surface.

nanoparticles (NPs). The SLB membrane is formed in the first step by wetting of the surface with lipid material originating from a multilamellar vesicle (MLV) suspension loaded into the microfluidic containers [8]. Following a washing step, the neutravidin-coated nanoparticles in aqueous suspension are pumped through the chamber across the deposited SLB. NPs bind in this step by an affinity reaction to the biotinylated SLB. We measured over time the change of resonance frequency as well as the change in the amplitude of the conductance at resonance for each step in the deposition experiment (figure 10).

The observed responses are showing the same trends as the measurements of the same system with the sensor design presented in part I. They confirm that frequency and magnitude of conductance can be used as independent complementary parameters of SAR sensor systems. More specifically, the SLB loading results in downshifts in frequency and conductance peak magnitude, while NP loading results in frequency downshift and conductance peak magnitude upshift. Accordingly, SLB deposition represents a mass loading with effect on the viscoelastic properties of the sensor surface, while the reaction with NP contributes to increased rigidity of the bio-layer, as indicated by the increased magnitude of conductance peak.

The measured response of the newly designed SAR sensor shows significantly improved sensitivity compared to the device presented in part I [8]. In table 2 a detailed comparison of the mass sensitivities of both devices is presented. The short-time response (seconds rather than minutes) of the new sensor to changes in loading can potentially also reveal additional information about the involved binding processes and will be investigated in a separate study.

**Table 2.** Comparison of mass sensitivities for different SAR devices.

Design: parameters:	Original (part I) freq./conduct.	Improved freq./conduct.
Air to water	−915 ppm/−5%	−2200 ppm/−27%
Water to buffer	−160 ppm/−1%	−315 ppm/−2%
Water to SLB	−65 ppm/0%	−130 ppm/−2%
SLB to SLB/NPs	−90 ppm/+2%	−160 ppm/+2%

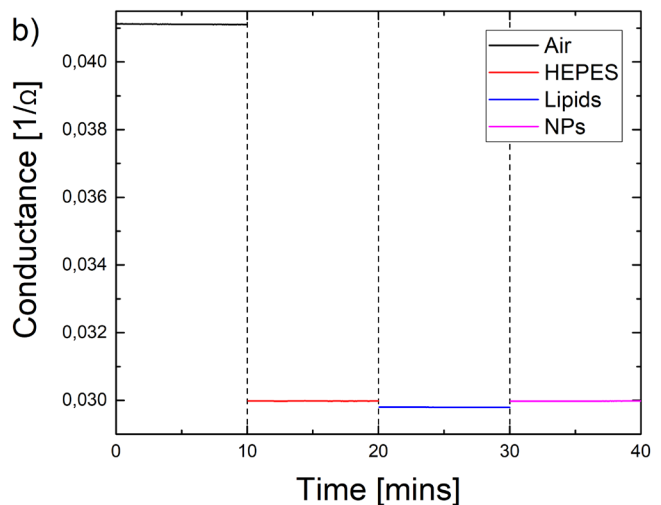
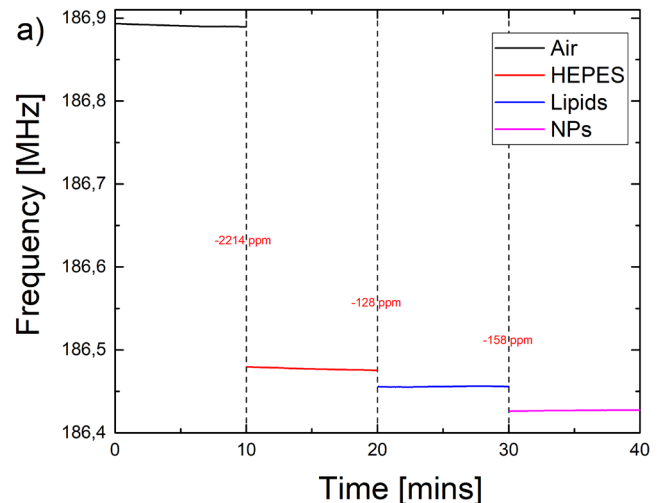


**Figure 10.** Time-resolved response of the SAR sensor subjected to the SLB deposition/affinity reaction sequence; (a) frequency shift (b) peak conductance magnitude shift.

### 3.3. Sensing of SLB transformations

Divalent calcium cations ( $\text{Ca}^{2+}$ ) are known to bind to negatively charged phospholipids, such as phosphatidylserine [14], and lead to a tighter packing of molecular lipid films, dehydration of lipids, as well as conformational changes to the lipid headgroups [15]. Generally, the fluidity of the membrane is to some extent reduced. Recent research has also shown that local exposure of lipid membranes in the low-tension regime (excess lipid material) to calcium ion concentrations in the range of 1–5 mM leads to a partial transformation of the planar membranes to



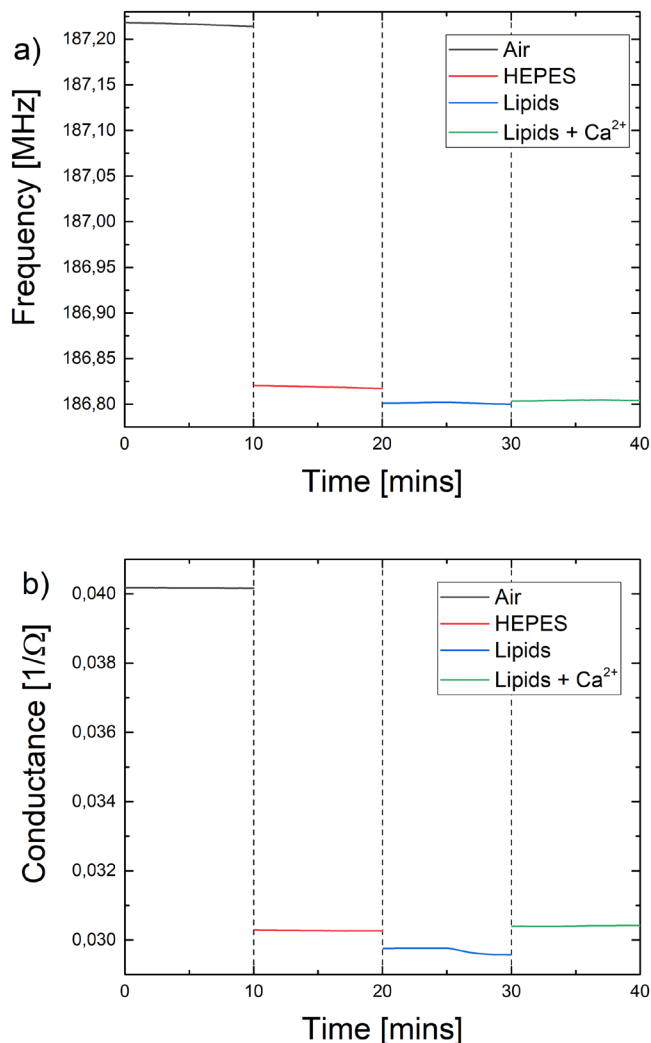


**Figure 11.** Time-resolved response of the SAR sensor subjected to a SLB reaction with  $\text{Ca}^{2+}$ ; (a) frequency shift (b) peak conductance magnitude shift.

nanotubular structures that extend into the aqueous medium but remain attached to the membrane [16]. This transformation, when it occurs on a surface-supported membrane, would effectively lead to a transfer of lipid material from an adhered surface film into the aqueous space above it, where parts of the lipid material float close to the membrane in a loosely connected regime. This should decrease the effective loading, owing to the 40 nm decaying length of the 180 MHz SH-SAW, resulting in a measurable increase in resonance frequency.

For our sensor, the 5 mM  $\text{Ca}^{2+}$  exposure of the SLB is accompanied by a frequency upshift of about 23 ppm, and a simultaneous conductance peak upshift of about 3% (figure 11). We attribute the upshift of both quantities to the above mentioned slightly reduced mass load, but also to increased rigidity of the calcium-rich SLB layer. The comparatively small frequency up-shift can be associated with the slight expected decrease in effective mass loading, while we attribute the up-shift in conductance peak magnitude to decreased losses, i.e. with layer rigidity. At this point we do not have any additional experimental data to verify this hypothetical mechanism, but our measurements provide evidence that the SAR sensor can be potentially useful for the characterization

of transformations of lipid membranes. Note that the length of the tubular protrusions depends on the availability of excess membrane material [16, 17], and can range from a few nanometers to several micrometers. In our case we estimate the range to be only within several tens of nm, as large lipid reservoirs are not available. The deposition of small multilamellar vesicles onto the surface in the first step may, however, provide sufficient excess lipid material to establish the low-tension regime required for tubulation to occur. This can in the future be verified by means of other film deposition methods, which would either lead to a high membrane tension and prevent the formation of tubes, or supply larger quantities of lipids in the form of large or giant multilamellar (onion shell) vesicles.

#### 4. Future trends in SAR sensor design

The design of SAR sensor can further be optimized in view of reducing the temperature sensitivity as well as integration with other functionalities. Here we discuss some straightforward approaches emanating from the specific SAR design.

We measured the temperature coefficient of the resonance frequency to be  $-83 \text{ ppm K}^{-1}$ , while the antiresonance frequency demonstrated a temperature dependence of about  $-72 \text{ ppm K}^{-1}$ . These numbers are typical for the  $\text{LiNbO}_3$  substrate and need to be reduced to improve upon the limit of quantification/detection. It is expected that reducing the temperature coefficient of frequency (TCF) will lead to a further significant reduction in measurement uncertainties. One simple way to achieve this would potentially be the subtraction of resonance from antiresonance frequencies. They exhibit close similarities in thermal response, while the difference in mass-sensitivity is remarkably large. Signal subtraction reduces the thermal sensitivity to  $-11 \text{ ppm K}^{-1}$ , while retaining a significant mass sensitivity. In a measurement environment with 0.1 K temperature tolerance, this translates in to a maximum  $-1.1 \text{ ppm}$  frequency shift, which is comparable to the noise level. More elaborate frequency subtraction techniques can readily eliminate the first order TCF in the sensor response.

Alternatively, the compensation of the thermal drift can be achieved by adding a  $\text{SiO}_2$  layer of about  $0.3\lambda$  thickness [18]. This technique has the additional advantage to electrically decouple the electrodes from the liquid and thus enable a robust SAR sensor design, where the IDT does not need to be separated from the liquid environment by a cavity. Theoretical estimations show that the effect of electrical short-circuiting on the surface of the SAR grating is a frequency downshift of about  $-1000 \text{ ppm}$ , while short-circuiting of the surface of the  $0.3\lambda$  thick  $\text{SiO}_2/\text{Au}$  strips/ $\text{LiNbO}_3$  composite is expected to induce a change of less than 0.3 ppm. Accordingly, SAR sensors with either an electrically screened or open-circuit top surface can be produced without any sacrifice in device performance, while enabling efficient compensation of the SAR thermal drift, and simplifying the microfluidic circuitry.

Last but not least, the new sensor design includes the capability for simultaneous low frequency ( $<1 \text{ MHz}$ ) electrochemical impedance spectroscopy (EIS). On-chip EIS employs the reflector strips in interdigitated split electrode geometry (figure 12). The split electrode topology of the

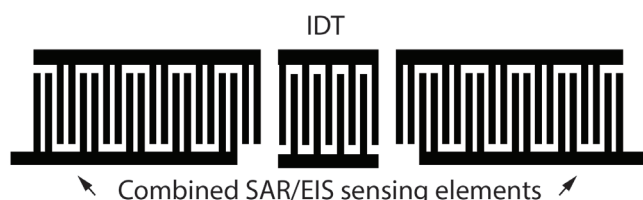


**Figure 12.** Schematic drawing of a suggested electrode configuration for an integrated SAR/EIS sensor.

reflectors is specifically suitable, since the SH-SAW experiences it as a short-circuited grating. Specifically, two neighboring electrodes distributed within a wavelength are connected electrically, therefore the SH-SAW does not induce potential over a pair of connected electrodes at resonance. Moreover, the EIS operates at a frequency where acoustic waves are not excited, thus both functionalities, i.e. acoustic sensing and EIS sensing, can be operated independently. Interdigitated electrodes are a common configuration in EIS sensing [19]. A proposed integration of EIS with SAR device is schematically shown in figure 12.

## 5. Conclusions

A ‘LEC’ design concept for a SAR in-liquid sensor has been demonstrated and its performance experimentally characterized. The acoustic wave confinement led to a sensitivity increase of >100%, which was determined by loading the sensor with a series of solutions of different  $\rho\eta$ . Time-resolved measurements of the sensor response confirmed stable operation with a limit of frequency detection of  $3\sigma < 1.5$  ppm, and the limit of conductance magnitude detection to be below 30 ppm. At anti-resonance, the SAW is strongly localized under the IDT, and exhibits a 2.3 times smaller mass-sensitivity as compared to resonance, while exhibiting similar thermal drift. This can be utilized for further improvement of the noise characteristics by canceling out thermal fluctuations in the measurement.

A microfluidics-enabled biomembrane-nanoparticle assay was further used to demonstrate that the sensor is capable of following multi-step bioaffinity processes in sample volumes of  $\sim 10 \mu\text{l}$ . In the context of 2D fluidic molecular films as sensing layer, the combined evaluation of frequency and conductance can reveal details about structural changes in the sensing layer, as shown for the  $\text{Ca}^{2+}$ -induced transformation of the sensor-surface-supported lipid membrane.

## Acknowledgments

We acknowledge the European Union (Horizon 2020 FET Open research grant, Project ID: 664786) and the Swedish Strategic Research Foundation (SSF).

## ORCID iDs

K Kustanovich <https://orcid.org/0000-0002-7762-7157>  
 V Yantchev <https://orcid.org/0000-0002-2696-1649>  
 B Ali Doosti <https://orcid.org/0000-0001-9149-0751>

## References

- [1] Go D B, Atashbar M Z, Ramshani Z and Chang H C 2017 Surface acoustic wave devices for chemical sensing and microfluidics: a review and perspective *Anal. Methods* **9** 4112–34
- [2] Wingqvist G, Bjurström J, Liljeholm L, Yantchev V and Katardjiev I 2007 Shear mode AlN thin film electro-acoustic resonant sensor operation in viscous media *Sensors Actuators B* **123** 466–73
- [3] Katardjiev I and Yantchev V 2012 Recent developments in thin film electro-acoustic technology for biosensor applications *Vacuum* **86** 520–31
- [4] Mirea T, Yantchev V, Olivares J and Iborra E 2016 Influence of liquid properties on the performance of S-0-mode Lamb wave sensors II: experimental validation *Sensors Actuators B* **229** 331–7
- [5] Gizeli E 2000 Study of the sensitivity of the acoustic waveguide sensor *Anal. Chem.* **72** 5967–72
- [6] Kondoh J 2013 A liquid-phase sensor using shear horizontal surface acoustic wave devices *Electr. Commun. Japan* **96** 41–9
- [7] Hohmann S, Kogel S, Brunner Y, Schmieg B, Ewald C, Kirschhofer F, Brenner-Weiss G and Lange K 2015 Surface acoustic wave (SAW) resonators for monitoring conditioning film formation *Sensors* **15** 11873–88
- [8] Kustanovich K, Yantchev V, Kirejev V, Jeffries G D M, Lobovkina T and Jesorka A 2017 A high-performance lab-on-a-chip liquid sensor employing surface acoustic wave resonance *J. Micromech. Microeng.* **27** 114002
- [9] Wingqvist G, Yantchev V and Katardjiev I 2008 Mass sensitivity of multilayer thin film resonant BAW sensors *Sensors Actuators A* **148** 88–95
- [10] Assouar M B, Kirsch P and Alnot P 2009 New Love wave liquid sensor operating at 2 GHz using an integrated micro-flow channel *Meas. Sci. Technol.* **20** 095203
- [11] Mirea T, Iborra E and Yantchev V 2016 S-0 Lamb wave resonators for in-liquid sensing: promising alternative to shear bulk acoustic wave devices 2016 *European Frequency and Time Forum (EFTF)* (<https://doi.org/10.1109/EFTF.2016.7477807>)
- [12] Vig J R 1991 On acoustic sensor sensitivity *IEEE Trans. Ultrason. Ferroelectr. Freq. Control* **38** 311
- [13] Morita T, Sugimoto M and Kondoh J 2009 Measurements of standard-viscosity liquids using shear horizontal surface acoustic wave sensors *Japan. J. Appl. Phys.* **48** 07GG15
- [14] Sinn C G, Antonietti M and Dimova R 2006 Binding of calcium to phosphatidylcholine-phosphatidylserine membranes *Colloid Surf. A* **282** 410–9
- [15] Melcrova A, Pokorna S, Pullanchery S, Kohagen M, Jurkiewicz P, Hof M, Jungwirth P, Cremer P S and Cwiklik L 2016 The complex nature of calcium cation interactions with phospholipid bilayers *Sci. Rep.* **6** 38035
- [16] Ali Doosti B, Pezeshkian W, Bruhn D S, Ipsen J H, Khandelia H, Jeffries G D M and Lobovkina T 2017 Membrane tubulation in lipid vesicles triggered by the local application of calcium ions *Langmuir* **33** 11010–7
- [17] Gozen I, Billerit C, Dommersnes P, Jesorka A and Orwar O 2011 Calcium-ion-controlled nanoparticle-induced tubulation in supported flat phospholipid vesicles *Soft Matter* **7** 9706–13
- [18] Matsuda S, Miura M, Matsuda T, Ueda M, Satoh Y and Hashimoto K-Y 2010 Investigation of  $\text{SiO}_2$  film properties for zero temperature coefficient of frequency SAW devices 2010 *IEEE Int. Ultrasonics Symp.* pp 633–6
- [19] Lisdat F and Schafer D 2008 The use of electrochemical impedance spectroscopy for biosensing *Anal. Bioanal. Chem.* **391** 1555–67